Research Square

Preprints are preliminary reports that have not undergone peer review.
They should not be considered conclusive, used to inform clinical practice,
or referenced by the media as validated information.

A Resilient Large-Piston Electrothermal Micromirror and Its Application in Handheld Fourier-Transform Near-Infrared Microspectrometers

Huikai Xie

hk.xie@bit.edu.cn

Beijing Institute of Technology

Hengzhang Yang

Beijing Institute of Technology

Qiangqiang Liu

Beijing Institute of Technology

Anrun Ren

Beijing Institute of Technology

Teng Pan

Beijing Institute of Technology

Yang Yang

Beijing Institute of Technology

Zhe Peng

Beijing University of Technology

Xiaoyi Wang

Beijing Institute of Technology https://orcid.org/0000-0002-6286-3085

Article

Keywords:

Posted Date: November 11th, 2026

DOI: https://doi.org/10.21203/rs.3.rs-11420924/v1

License: This work is licensed under a Creative Commons Attribution 4.0 International License.
Read Full License

Additional Declarations: There is no conflict of interest

A Resilient Large-Piston Electrothermal Micromirror and Its Application in Handheld Fourier-Transform Near-Infrared Microspectrometers

Hengzhang Yang[1,2], Qianqiang Liu[1,2], Anrun Ren[1,2], Teng Pan[1,2], Yang Yang[1,2], Zhe Peng[4], Xiaoyi Wang[1,2,3], Huikai Xie[1,2,3,*]

Correspondence: hk.xie@bit.edu.cn

Abstract

Handheld Fourier-transform near-infrared (FTNIR) microspectrometers demand MEMS micromirrors capable of generating large piston displacement (LPD) for high spectral resolution, alongside the strict mechanical robustness required for field deployment. However, conventional electrothermal actuators rely on rigid and brittle inorganic dielectrics (e.g., Al-SiO_2), which severely suffer from impact-induced fracture and inherently restrict the maximum actuation stroke. Here, we demonstrate a highly robust LPD electrothermal micromirror driven by an aluminum-photosensitive polyimide (Al-PSPI) bimorph actuator. The device features a 1 mm × 1 mm square mirror within a compact 1.85 mm × 1.85 mm footprint. Leveraging the superior mechanical compliance and resilience of PSPI, the actuators can survive drop heights up to 1.9 m, a 25-fold improvement over conventional Al-SiO_2 bimorph counterparts. The micromirror achieves a maximum piston displacement exceeding 450 μm at an ultra-low driving voltage of 7.5 V, exhibiting a fundamental resonance frequency of ~588 Hz and a rapid response time of ~30 ms. To validate its practical utility, the micromirror was integrated into a compact, 350-gram handheld FTNIR prototype. The compact FTNIR achieves a spectral resolution of 26.2 cm^{-1} and covers a wide spectral range from 800 nm to 2500 nm, and it maintains stable operation under rigorous logarithmic sweep vibration testing (1 g, 20 – 2000 Hz, 12 min). This work establishes a versatile actuator design paradigm that fundamentally resolves the structural fragility of large-stroke MEMS mirrors, paving the way for next-generation portable hyperspectral imaging and highly reliable interferometric systems operating in extreme environments.

Introduction

Fourier-transform near-infrared (FTNIR) microspectrometer is widely used for broadband spectral analysis. In a typical Michelson configuration, an interferogram is generated by modulating the optical path difference (OPD), and the spectrum is reconstructed through Fourier transformation[1]. Owing to its non-destructive nature, high sensitivity, and rapid acquisition, FTNIR supports many applications, including

biomedical analysis[2-4], material identification[5-7], and environmental monitoring[8-10]. However, conventional benchtop FTNIR instruments are often bulky, expensive, and sensitive to environmental disturbances, which limits their deployment to centralized laboratories[11,12]. Emerging scenarios require on-site measurements, such as outdoor inspection and real-time material screening (Fig. 1a), where sample transport increases costs and delays decision-making. This motivates the development of handheld FTNIR systems that are compact and robust enough for routine field operation[13,14].

Advances in microelectromechanical systems (MEMS) have enabled miniaturized FTNIR architectures that reduce size, weight, and power consumption while preserving the interferometric advantage[15,16]. In such systems, a MEMS micromirror is responsible for OPD modulation, thereby determining the attainable spectral resolution. Electrothermal micromirrors are particularly attractive for handheld FTNIR because they can provide large piston displacements at low driving voltages, simplifying the actuation electronics and improving operational safety. In addition, their small footprint and high fill factor reduce the optical-module volume and relax packaging constraints[17-21].

Despite these advantages, mechanical robustness remains a major obstacle. Practical handheld devices are routinely exposed to drops, shocks, and vibrations; the micromirror must tolerate these loads without cracking or performance drift. Many electrothermal micromirrors employ Al-SiO_2 bimorph actuators (Fig. 1b) to exploit the large thermal-expansion mismatch for efficient actuation[22,23].While the low thermal conductivity of SiO_2 serves as the thermal isolation anchor[24,25], its inherently brittle nature makes it prone to impact-induced cracking. Consequently, conventional designs often fail drop tests from only a few centimeters[26], which severely restricts their applicability in handheld FTNIR. Several strategies have been explored, including structural reinforcement, protective packaging, and alternative material stacks[27-30]. These approaches often increase fabrication complexity or compromise system integration, and they still do not fully address the robustness required for field deployment.

Furthermore, achieving high spectral resolution in a handheld form factor requires maximizing the usable piston stroke (and thus the OPD) within a limited footprint. The high Young's modulus and brittleness of SiO_2 restrict the maximum actuation stroke, which often remains comparable to or smaller than the initial release-induced elevation[17,18]. Here, we address both the robustness and vertical displacement challenges by introducing a lateral-shift-free (LSF) electrothermal micromirror that replaces the conventional Al-SiO_2 bimorph with an Al-PSPI bimorph. The ductile and compliant nature of PSPI increases energy dissipation under impact and provides a substantially larger deformation margin. Consequently, the proposed device supports a large OPD at a low driving voltage while maintaining strict mechanical integrity under severe vibration, shock, and drop conditions. We further demonstrate system-level relevance by integrating the micromirror into a handheld FTNIR prototype (with a mass of 350-gram) to achieve accurate spectral measurements, offering a highly practical route toward field-deployable interferometric spectroscopy.

Results

Concept and system integration of the Al-PSPI micromirror in FTNIR

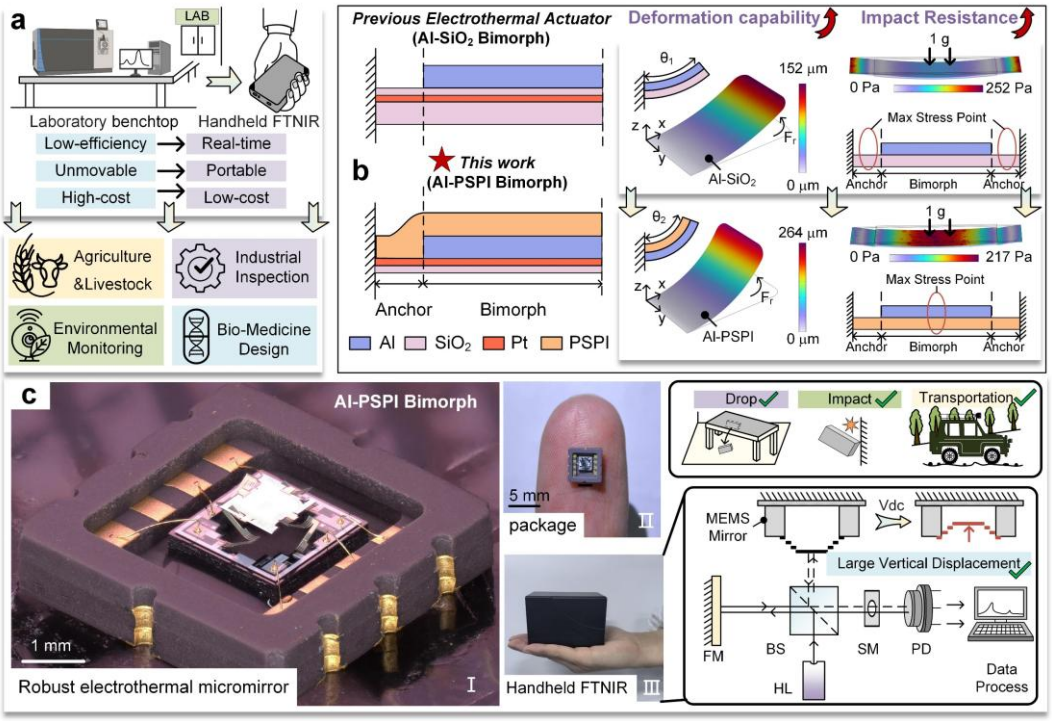


Fig. 1. Conceptual overview of the impact-resilient micromirror and the handheld FTNIR system. a, Motivation and representative application scenarios for handheld FTNIR system. **b,** Structural and performance comparison between the conventional Al-SiO_2 bimorph actuator and the proposed Al-PSPI bimorph actuator, highlighting the enhanced deformation capability and reduced stress concentration. **c,** Optical configuration of the packaged micromirror and the proposed handheld FTNIR system. BS: beam splitter; FM: fixed mirror; HL: halogen lamp; SM: sample; PD: position detector.

Improving impact resistance of the actuator must fundamentally originate at the materials level. Specifically, we replace the brittle SiO_2 layer in conventional bimorphs with a compliant PSPI layer to form an Al-based actuator with an expanded deformation margin and enhanced energy dissipation. Beyond providing a large thermal-expansion mismatch with Al, PSPI exhibits excellent lithographic pattern capability, process compatibility, and functions as a low-thermal-conductivity isolation anchor to suppress heat leakage. Thin SiO_2 is retained strictly for passivation and electrical isolation (Fig. 1b). To validate the structural advantages, finite element method (FEM) simulations were conducted comparing the Al-SiO_2 and Al-PSPI bimorphs under identical geometric boundaries and applied loads. Under a stress-induced load (F_r=200 MPa in this case as an example), the Al-PSPI bimorph exhibited significantly greater vertical displacement than its Al-SiO_2 counterpart, demonstrating a superior capacity for large-stroke actuation. Crucially, in impact resistance tests subjecting the fixed structures to a vertical acceleration (1 g in this case as an example), the maximum stress within the

Al-SiO_2 bimorph was heavily concentrated at the rigid anchor points, which matches the typical fracture locus observed in conventional devices. In sharp contrast, substituting SiO_2 with PSPI substantially reduced the peak stress and shifted the stress distribution away from the vulnerable anchors toward the center of the bimorph beam, fundamentally enhancing the structural survivability.

Fig. 1c schematically shows the self-developed FTNIR based on the Al-PSPI bimorph actuator. The packaged chip footprint is merely 5 mm × 5 mm with a mass of 66 milligram. The fully integrated handheld FTNIR instrument measures 90 mm × 55 mm × 58 mm with a mass of 350 gram. The combined ductility of Al and the high compliance of PSPI not only imbue the handheld system with exceptional shock resistance but also unlock a significantly larger OPD for spectral measurements, directly improving the attainable optical resolution.

Design of the Robust Al-PSPI Micromirror

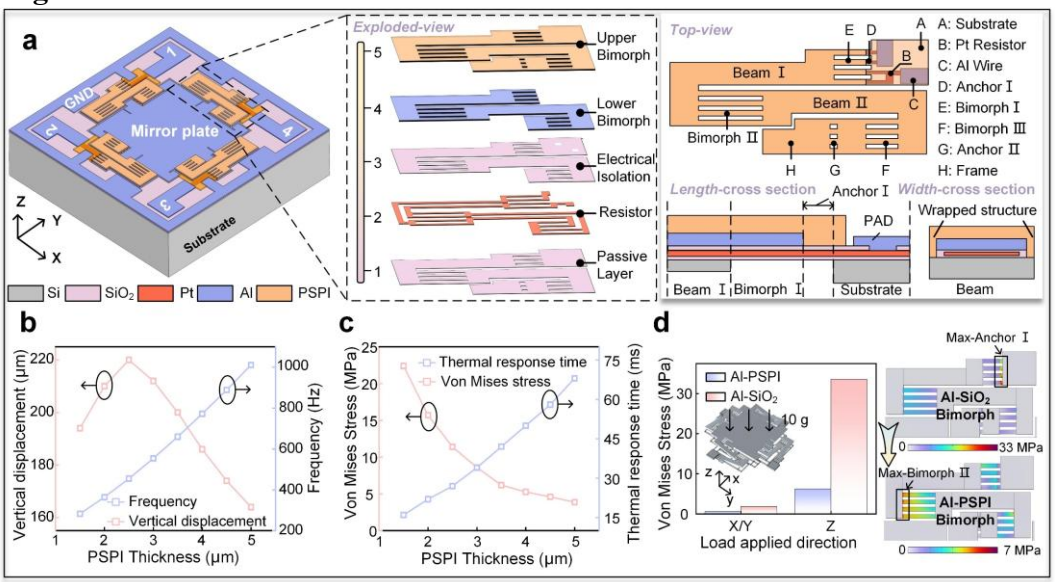


Fig. 2. Design of the proposed micromirror. a, Schematic 3D view of the proposed Al-PSPI bimorph-based micromirror. **b~c**, Finite-element simulations showing the dependence of key micromirror metrics on PSPI thickness (including resonant frequency, piston displacement, thermal response time and von Mises stress). **d,** Comparison of von Mises stress distributions for the two bimorph designs under representative impact loading.

Serving as the core OPD modulator of the handheld FTNIR, the MEMS micromirror necessitates a meticulously coordinated thermomechanical and electrical design. As illustrated in Fig. 2a, the proposed micromirror features a central square mirror plate suspended by four symmetrically arranged peripheral actuators. This four-quadrant topology inherently enables pure piston motion for FTNIR operation. Each actuator consists of three bimorph segments linked by two rigid straight beams, with an embedded serpentine Pt resistor providing Joule heating for electrothermal actuation. To ensure high structural flatness and compensate for inherent residual stress-induced curling, the bimorph II segment is designed to be exactly twice the length of the

proximal and distal segments. The intermediary straight beams not only enhance structural robustness but also contribute to angular amplification during displacement.

To leverage the advantages of a multi-layer stack while mitigating mechanical vulnerabilities, the thicknesses of the passive films must be rigorously controlled. Specifically, the thickness of both the SiO_2 passivation and insulating layers is meticulously constrained to a mere 100 nm. From a functional perspective, this ultrathin passivation layer is sufficient to protect the underlying Ti adhesion layer from severe gas corrosion during the structural release phase, which is vital for long-term device reliability in ambient environments. Concurrently, the insulating layer guarantees robust dielectric isolation between the Pt heater and the Al structural layer, ensuring that electrical power is efficiently converted into Joule heating without leakage. From a thermomechanical perspective, maintaining this 100 nm ultrathin profile essentially eliminates the parasitic stiffness typical of brittle SiO_2. Consequently, it introduces virtually no mechanical impedance, fully preserving the large deformation capability and the superior impact resilience of the compliant Al-PSPI architecture.

To maximize space utilization and the optical fill factor, we implement a folded-beam architecture rather than a conventional linear cantilever geometry. Device dimensions were carefully tailored to accommodate the isotropic release process and the resulting lateral under-etch. Utilizing a 20 μm silicon-on-insulator (SOI) device layer, the bimorph width is set to 20 μm, while the minimum structural beam width is conservatively defined as 80 μm (detailed parameters in Tab. S1). Assuming an equal lateral-to-vertical etch rate, this geometry guarantees that at least 50% of the underlying silicon remains intact after the isotropic release, preserving essential structural rigidity. Consequently, the total footprint of the micromirror is constrained to 1.8 mm × 1.8 mm, yielding a mirror fill factor exceeding 25%. To further bolster interfacial adhesion and provide multidirectional impact buffering, the compliant PSPI layer is intentionally patterned wider than the underlying Al layer, effectively encapsulating the actuator beams (Fig. 2a, cross-section detail).

The thickness of the PSPI layer dictates the ultimate performance and robustness of the bimorph. FEM simulations were utilized to optimize this critical parameter. As shown in Fig. 2b, increasing the PSPI thickness monotonically raises the resonant frequency. However, the attainable vertical displacement exhibits a distinct peak, highlighting a fundamental trade-off between dynamic stiffness and actuation efficiency. Furthermore, Fig. 2c reveals that a thicker PSPI layer significantly suppresses the peak von Mises stress, which enhances mechanical robustness. However, this incurs a penalty in thermal response time due to increased thermal inertia. Although the theoretical maximum deformation is achieved at a PSPI thickness of 2.5 μm, such a relatively thin layer poses step-coverage challenges over the underlying multi-layer topography during microfabrication, potentially compromising device yield. Balancing optimal electromechanical performance with robust manufacturability, a final PSPI thickness of 3.5 μm was selected. Finally, with the optimized geometry established, we evaluated the multidirectional impact resistance under severe acceleration loads (10 g as an example). As summarized in Fig. 2d, the proposed Al-PSPI bimorph demonstrates starkly superior impact tolerance across all three orthogonal axes when compared to the

conventional Al-SiO_2 architecture.

Characteristic of the Al-PSPI based micromirror

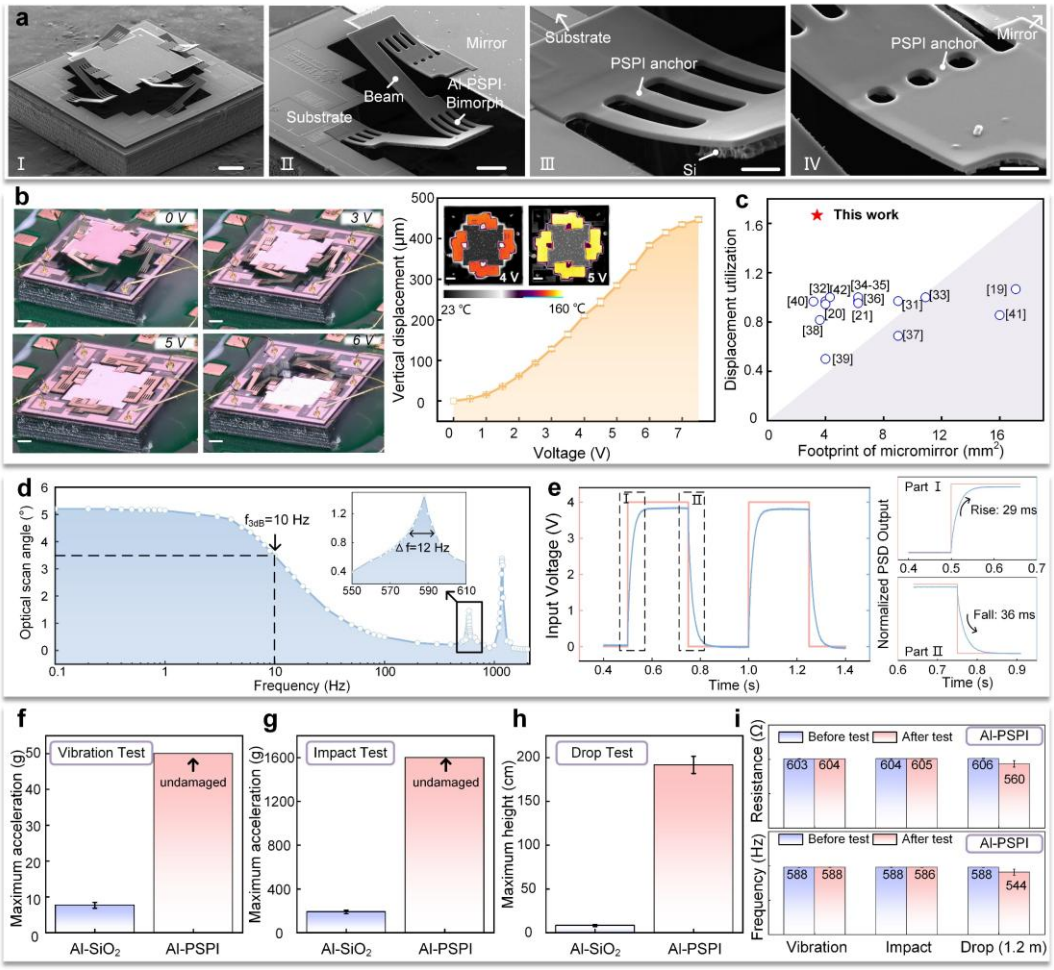


Fig. 3 Device characteristics and impact tolerance of the Al-PSPI micromirror. a, SEM images of the released micromirror. Scale bars, 250 μm, 100 μm, 25 μm, and 25 μm (from left to right). **b,** Vertical displacement as a function of applied DC voltage (downward displacement defined as positive). Scale bars, 200 μm. **c,** Displacement utilization ratio versus device footprint, benchmarked against representative electrothermal micromirrors[19-21,31-42]. **d,** Frequency response with a sinusoidal signal from 0.1 Hz to 2000 Hz. **e,** Step response under square-wave driving. **f~h**, Reliability test results, including vibration (f), impact (g), and drop (h), for micromirrors with Al-PSPI and Al-SiO_2 bimorph actuators. **i,** Changes in resonant frequency and actuator resistance of Al-PSPI micromirrors after vibration, impact and drop tests.

The micromirror was fabricated on a silicon-on-insulator (SOI) wafer using a combined surface and bulk micromachining process (Fig. S1 and Table S2). Fig. 3a illustrates the scanning electron microscopy (SEM) images of the released electrothermal micromirror employing the Al-PSPI bimorph architecture. Driven by inherent residual stress, the mirror plate exhibits an initial out-of-plane lift of ~270 μm. Statistical analysis across ten identically fabricated samples reveals a tight device-to-

device variation of less than 10 μm (Table S3), indicating high process uniformity. Magnified views confirm well-defined PSPI anchors with conformal step coverage and robust adhesion at the target PSPI thickness of 3.6 μm (Fig. S2). As strategically designed, residual silicon is intentionally preserved beneath the actuator beams to provide supplementary mechanical rigidity. Bottom-view inspections further verify a uniform undercut depth of ~20 μm, corresponding to a ~50% retention of the silicon width beneath the beams (Fig. S3). For benchmarking purposes, conventional Al-SiO_2 bimorph micromirrors were co-fabricated on the same wafer, exhibiting a comparatively smaller initial lift of ~190 μm (Fig. S4 and Table S4).

Device performance was characterized using a batch of ten micromirrors with closely matched electrical resistance (600 ± 5 Ω; Table S5). In FTNIR, the maximal piston displacement dictates the achievable OPD, thereby establishing the fundamental upper bound for spectral resolution. Fig. 3b plots the vertical displacement as a function of the applied DC voltage (downward motion defined as positive). The displacement scales monotonically with the ultra-low driving voltage, exhibiting near-linear behavior across a broad range from 95 to 390 μm. The mirror plate traverses the substrate reference plane at ~5 V and continues its downward trajectory. Remarkably, a maximal displacement magnitude of ~450 μm is attained at merely 7.5 V. While larger strokes could theoretically be achieved by elongating the actuator beams, such geometric scaling inevitably sacrifices the optical fill factor, which is a critical detriment for handheld systems. Therefore, extracting a massive piston stroke within a constrained footprint is paramount. The exceptional ductility of Al combined with the high compliance of PSPI yields a significantly larger deformation margin than conventional Al-SiO_2 designs (Table S6). To quantitatively evaluate this efficiency, we define the displacement utilization ratio as the maximum operational stroke divided by the initial residual-stress-induced lift. As depicted in Fig. 3c, the proposed Al-PSPI micromirror achieves a remarkably high utilization ratio of 1.67 (Table S7) while maintaining a highly compact footprint of 1.85 mm × 1.85 mm, vastly outperforming representative state-of-the-art Al-SiO_2 designs. Conventional inorganic bimorphs rarely exceed their initial lift; further actuation typically precipitates irreversible yield or catastrophic fracture due to the high stiffness and brittleness of the protective SiO_2 layer. In our paradigm, Al and PSPI function as the primary active thermomechanical components, with ultra-thin SiO_2 relegated purely to passivation and dielectric isolation, thereby nullifying its mechanical penalty. Infrared thermography (Fig. 3b, inset) reveals a uniform temperature distribution strictly confined to the driving beams, confirming the excellent thermal isolation enabled by the symmetric anchor design. Furthermore, the operating temperature of the actuator was quantitatively monitored by measuring the temperature coefficient of resistance (TCR) of the Pt resistor (Fig. S5), which reached ~160 °C at an applied voltage of 5 V. Additional static and dynamic characteristics of the Al-PSPI micromirror are detailed in Fig. S6.

Dynamic performance evaluation reveals two resonant peaks within the 0.1-2000 Hz range (Fig. 3d), with dominant modes at 588 Hz (piston) and 1180 Hz (tip-tilt). As even higher-order modes show minimal responsivity, we limited our frequency response up to 2000 Hz. Response time was characterized using a position-sensitive

detector (PSD) under square-wave driving at 2 Hz with a 50% duty cycle and a 4 V AC excitation. As shown in Fig. 3e, the device exhibits a rise time of 29 ms and a fall time of 36 ms. The slightly longer fall time is attributed to slower thermal relaxation during cooling and the thermal inertia of the mirror plate. The device exhibits a 3dB cutoff frequency of 10 Hz, corresponding to a thermal time constant (τ) of 15.9 ms, calculated from $\tau = 1/(2\pi \cdot f_{3dB})$. Quality factor (Q) analysis yields $Q \approx 49$, derived from the fundamental resonance frequency (f_0) and full width at half maximum ($\Delta f \approx 12$ Hz, inset of Fig. 3d). Thus, the condition $\tau \cdot f_0 > Q/2\pi$ explains the absence of overshoot in the actuator response[43].

To quantify impact tolerance, we conducted three reliability tests that emulate transport-induced vibration, transient mechanical impact, and accidental drops. Conventional Al-SiO_2 bimorph micromirrors were evaluated in parallel as controls. For each test, ten devices of each type were randomly selected, and device integrity was inspected under an optical microscope before and after testing. After each test, five Al-PSPI devices were randomly chosen for electrical and mechanical readouts. Actuator resistance and resonance frequency were measured to quantify performance drift.

Vibration test. Continuous vibration is common during transportation and mobile deployment. Vibration testing was performed using a calibrated vibration system (SignalCalc 901 DP; Fig. S7), where micromirrors were driven along the out-of-plane axis and monitored by an accelerometer. As summarized in Fig. 3f, Al-SiO_2 devices failed at ~7 g, whereas Al-PSPI devices showed no actuator fracture or mirror detachment up to 50 g.

Impact test. Transient impact tolerance was evaluated using an impact table (OK-s-10; Fig. S8). Devices were mounted vertically and subjected to controlled drop-induced impacts. The peak shock load was set to 1600 g, corresponding to an equivalent free-fall height of ~1.3 m under the given impact profile. As shown in Fig. 3g, Al-SiO_2 devices withstood shocks only up to ~190 g, whereas Al-PSPI devices exhibited no observable structural damage even at 1600 g.

Drop test. Free-fall tests were performed on packaged devices to emulate accidental drops (Fig. S9). Both device types were packaged in a transistor outline (TO) can with a transparent glass cap, and the packaged mass was ~0.88 g. Samples were dropped onto an epoxy-coated floor from increasing heights. As shown in Fig. 3h, Al-SiO_2 devices survived drop heights up to 7 cm, whereas Al-PSPI devices tolerated drop heights up to ~190 cm, representing an approximately 25-fold improvement. Post-failure inspection (Figs. S10 and S11) revealed different failure modes. Al-SiO_2 devices predominantly fractured at the SiO_2 anchor regions, while Al-PSPI devices failed mainly at the second bimorph segment, consistent with the stress concentration predicted in Fig. 1g.

Post-failure diagnostics (Figs. S10 and S11) validated our theoretical models: Al-SiO_2 devices predominantly fractured at the rigid SiO_2 anchor boundaries, whereas ultimate yielding in Al-PSPI devices was redirected to the central bimorph segment, precisely matching the stress-distribution shift predicted via FEM (Fig. 2d). Finally, the operational stability of the Al-PSPI devices post-testing was excellent. As detailed in Fig. 3i, actuator resistance and resonance frequency drifted by less than 1% following

the 50 g vibration and 1600 g shock tests. Post-1.2 m drop test, the parameter variation remained well within 5%, comfortably satisfying the stringent operational bounds implied by the JESD22-B103B standard.[44]. Additional drop heights of 1.5 m and 1.8 m were also evaluated (Fig. S12), where variations increased to above 30% and 55%, respectively. Compared with controlled vibration and shock tests, the drop test exhibits larger scatter, which is expected because failure outcomes are sensitive to landing angle and contact dynamics.

The spectra test of the handheld miniaturized FTNIR

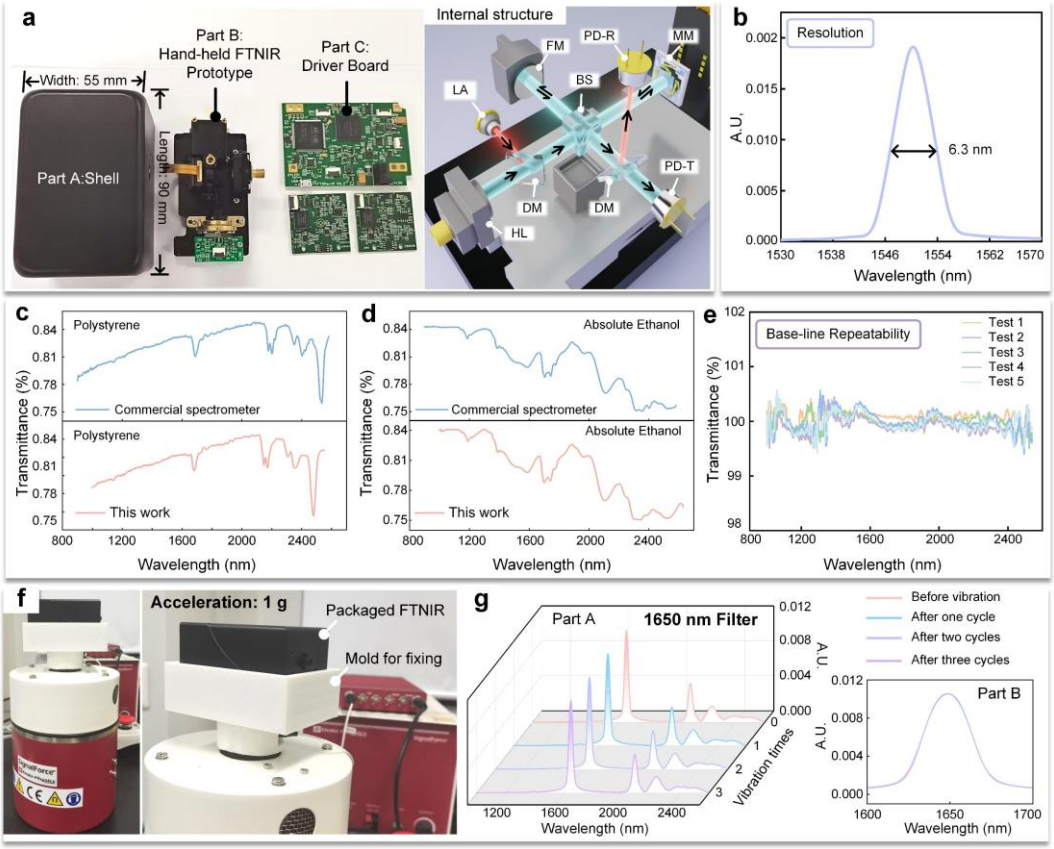


Fig. 4. Handheld FTNIR prototype enabled by the Al-PSPI micromirror and validation of practical spectral identification. **a,** Photograph of the handheld FTNIR prototype (90 mm × 55 mm × 58 mm; 350-gram), and key components of the proposed handheld FTNIR. BS, beam splitter; DM, dichroic mirror; LA, reference laser; FM: fixed mirror; HL, halogen lamp; MM, MEMS micromirror; PD-T, signal photodetector; PD-R, reference photodetector. Scale bar: 1 cm. **b,** The spectrometer's resolution at a wavelength of 1550 nm. **c~d**, Spectral identification of two representative samples, and the data are compared with a commercial portable spectrometer (NIR-Quest) as a reference. **e,** Baseline stability under no-load conditions, evaluated from five repeated measurements (normalized transmittance; fluctuation within ±0.5%). **f,** Vibration test setup of the FTNIR prototype. **g,** Comparison of test results of filter wavelength after vibration tests.

To validate spectral identification under practical operation, we integrated the Al-PSPI micromirror into the self-developed handheld FTNIR. Fig. 4a summarizes the key

components of our handheld FTNIR, which is built on a Michelson-type micro-interferometer. Broadband illumination, after interacting with the sample, is split by a beam splitter (BS) and directed to a fixed mirror (FM) and a MEMS micromirror (MM). The two reflected beams recombine at the BS and are routed to the signal photodetector (PD-T), where an interferogram is recorded and subsequently converted into the spectrum through Fourier transformation. In practice, non-uniform micromirror motion can lead to non-uniform OPD sampling and result in spectral reconstruction error[38,39]. To address this issue, we also introduce a reference channel using a wavelength-stabilized laser (LA) and an additional photodetector (PD-R), which enables real-time calibration of the sampling process (as shown in Figs. 13-15).

Fig. 4b shows the recovered spectrum of the reference laser, where the measured spectral resolution is 6.3nm at 1550 nm. We then assessed material identification using two representative samples, including a polystyrene film and anhydrous ethanol (setup in Fig. S16). A commercial portable spectrometer (NIR-Quest) was used as a reference. Figs. 4c~d compare the reconstructed spectra obtained by our handheld FTNIR with those from the reference instrument. The Al-PSPI micromirror-based FTNIR reproduces the key spectral features with comparable wavelength agreement and identification accuracy, while reducing the instrument volume to approximately one third of the reference unit (based on external dimensions of 182 mm × 110 mm × 47 mm). This compact form factor, together with the demonstrated reconstruction fidelity, supports the use of the proposed platform for portable, real-time, on-site spectroscopic analysis.

After sample measurements, we evaluated baseline stability under no-load conditions by acquiring five repeated datasets. As shown in Fig. 4e, the normalized transmittance remains stable across the full spectral range, with fluctuations confined within ±0.5%, indicating good system stability. Furthermore, a custom 3D-printed fixture was designed to secure the FTNIR prototype for the test. Vibration tests were performed using a SignalCalc 901 DP system. To accommodate the system's load capacity, the acceleration load was set to 1 g (refer to Hamamatsu[45]) during a 12-minute test cycle, with the frequency sweeping from 20 Hz up to 2000 Hz and back to 20 Hz. The experimental setup is illustrated in Fig. 4f. A total of three consecutive test cycles were conducted. Following each cycle, a 1650 nm optical filter was employed to characterize the operational stability of the prototype, as shown in Fig. 4g. The results demonstrate that the prototype exhibits accurate recognition capability (part A) and maintains the robust stability after continuous 1 g vibrational loading, with the center wavelength fluctuating by no more than 0.5 nm (part B).

Discussion and Conclusion

In this work, we developed an Al-PSPI electrothermal micromirror for handheld FTNIR and demonstrated its design, fabrication, device characterization, impact tolerance, and system-level integration. The results highlight three key advantages. First, the Al-PSPI based micromirror provides a large piston-mode stroke at low voltage,

which increases the available OPD without sacrificing a compact footprint. Second, the Al-PSPI bimorph markedly improves tolerance to vibration, shock, and drops, addressing a practical reliability bottleneck that has limited the deployment of electrothermal MEMS micromirrors in mobile and field settings. Third, the device remains compatible with a straightforward driving scheme and supports stable interferogram acquisition when combined with feedback control for tip-tilt suppression.

Quantitatively, the micromirror achieves a maximum vertical displacement over 450 μm within a 1.85 mm × 1.85 mm footprint and reaches a displacement utilization ratio of 1.67. The device maintains mechanical integrity under 50 g vibration, 1600 g shock, and ~1.9 m drop tests. These comprehensive quantitative evaluations confirm that the newly implemented Al-PSPI bimorph combination achieves a remarkable, concurrent enhancement in both large-stroke deformation capability and extreme impact resistance.

At the device level, the substantial OPD enabled by the bare chip yields an impressive spectral resolution of 0.7 nm @ 532 nm (as shown in Fig. S15). When integrated into a 350-gram handheld prototype, the system achieves a spectral resolution of 6.3 nm @ 1550 nm, and the material-identification accuracy comparable to a commercial portable spectrometer. Together, these results support a general design principle for field-deployable interferometric instruments: combining a ductile metal layer with a compliant polymer bimorph can simultaneously expand deformation margin and suppress brittle fracture under impact. Beyond the handheld FTNIR demonstrated here, the same combination of large stroke and mechanical robustness is promising for other compact scanning platforms, such as optical coherence tomography and LiDAR. The representative scanning trajectories in Fig. S17 further illustrate stable actuation under practical driving conditions.

Long-term stability remains an important consideration for polymer-enabled electrothermal actuators. Organic films can exhibit gradual drift under sustained electrothermal cycling, and their properties may be influenced by ambient moisture. In this study, long-term cycling tests were performed on both Al-PSPI and Al-SiO_2 micromirrors (Fig. S18 and Tab. S8). By tracking displacement-voltage characteristics, we observe that after 5 million continuous actuation cycles, the drift rate of the Al-PSPI device exceeds that of the Al-SiO_2 control by more than a factor of two. Here, drift is defined as the ratio between the displacement change and the initial displacement. The observed drift is consistent with time-dependent polymer stress relaxation and creep, potential interfacial fatigue, and moisture-related property variations under repeated electrothermal loading. To reduce the impact of drift on measurement accuracy, future systems can incorporate on-chip position sensing and closed-loop negative-feedback control to stabilize piston displacement during operation. Device-level strategies such as moisture-barrier or hermetic packaging, polymer conditioning or annealing, and duty-cycle-optimized driving are also expected to mitigate drift while retaining the robustness benefit. In addition, thermal management and power budgeting should be considered at the system level because electrothermal actuation involves elevated operating temperatures.

By integrating a compliant polymer layer directly into the actuator stack, this work

fundamentally breaks the long-standing limitation of mechanical fragility in large-stroke MEMS micromirrors. This paradigm shift not only enables ultra-robust, portable FTNIR implementations but also redefines the hardware baseline for a broader class of miniaturized interferometric systems, such as next-generation aerospace instruments and field-deployable spectrometers, that demand extreme reliability under rigorous operational conditions.

Materials and method

PSPI Material

The PSPI used in this study was a commercial product purchased from Nantong Jing-Ai Microelectronics Co., Ltd. (Nantong, China). Further details about the material are available at http://www.jing-ai.com/a/about.

Fabrication process

The micromirrors were fabricated on silicon-on-insulator (SOI) wafers utilizing a combined surface and bulk micromachining technique. The detailed fabrication sequence is illustrated in Fig. S1.

Acknowledgment

Funding: This work is supported by National Science and Technology Planning Project (2023YFB3507300); National Natural Science Foundation of China (U24A20301, 62350710218, 6231101499); Beijing Natural Science Foundation (1S24084);

Author Details

[1]State Key Laboratory of Chips and Systems for Advanced Light Field Display, School of Integrated Circuits and Electronics, Beijing Institute of Technology, Beijing 100081, China.

Hengzhang Yang, Qiangqiang Liu, Anrun Ren, Teng Pan, Yang Yang, Xiaoyi Wang, Huikai Xie

[2]Engineering Research Center of Integrated Acoustic-opto-electronic Microsystems (Ministry of Education of China), Beijing 100081, China.

Hengzhang Yang, Qiangqiang Liu, Anrun Ren, Teng Pan, Yang Yang, Xiaoyi Wang, Huikai Xie

[3]Chongqing Institute of Microelectronics and Microsystems, Beijing Institute of Technology, Chongqing 400030, China.

Xiaoyi Wang, Huikai Xie

[4]School of Integrated Circuits, Beijing University of Technology, Beijing 100124, China.

Zhe Peng

Author Contributions

H.Y. designed, fabricated, characterized the devices and carried out the experiment. Q.L., A.R., T. P., Z. P., Y. Y., and X. W. assisted in the experiment. X.W. and H. X. provided guidance to the experiment. H.Y. wrote the manuscript. H.X. supervised the project. H. X. revised the manuscript with contributions from all other co-authors.

Corresponding Author

Huikai Xie; hk.xie@bit.edu.cn

Conflict of interest

The authors declare no competing interests.

Data availability

The data that support the findings of this study are available from the corresponding author upon reasonable request.

Ethics approval and consent to participate

Not applicable

Reference

1 Shang, L. *et al.* Time-resolved photon counting Fourier-transform micro-spectroscopy enables simultaneous Raman and fluorescence lifetime imaging. *Light: Science & Applications* **14**, 378 (2025).

2 Amenabar, I. *et al.* Hyperspectral infrared nanoimaging of organic samples based on Fourier transform infrared nanospectroscopy. *Nat. Commun.* **8**, 14402 (2017).

3 Mistek-Morabito, E. & Lednev, I. K. Discrimination between human and animal blood by attenuated total reflection Fourier transform-infrared spectroscopy. *Communications Chemistry* **3**, 178 (2020).

4 Bevilacqua, C. & Prevedel, R. Full-field Brillouin microscopy based on an imaging Fourier-transform spectrometer. *Nature Photonics* **19**, 494-501 (2025).

5 Dong, D. *et al.* Analyzing Strawberry Spoilage via its Volatile Compounds Using Longpath Fourier Transform Infrared Spectroscopy. *Sci Rep* **3**, 2585 (2013).

6 Wang, Y.-D. *et al.* Discrimination of foodborne pathogenic bacteria using synchrotron FTIR microspectroscopy. *Nuclear Science and Techniques* **28**, 49 (2017).

7 Leite, A. I. N. *et al.* FTIR-ATR spectroscopy as a tool for the rapid detection of adulterations in butter cheeses. *LWT* **109**, 63-69 (2019).

8 Erfan, M. *et al.* On-Chip Micro–Electro–Mechanical System Fourier Transform Infrared

(MEMS FT-IR) Spectrometer-Based Gas Sensing. *Appl. Spectrosc.* **70**, 897-904 (2016).
9 Cai, F., Lu, W., Shi, W. & He, S. A mobile device-based imaging spectrometer for environmental monitoring by attaching a lightweight small module to a commercial digital camera. *Sci Rep* **7**, 15602 (2017).
10 Wang, Y. *et al.* The impact of biodegradable plastics on methane and carbon dioxide emissions in soil ecosystems: a Fourier transform infrared spectroscopy approach. *Sci Rep* **15**, 7678 (2025).
11 Yang, Z., Albrow-Owen, T., Cai, W. & Hasan, T. Miniaturization of optical spectrometers. *Science* **371**, eabe0722 (2021).
12 Yang, Z. *et al.* Single-nanowire spectrometers. *Science* **365**, 1017-1020 (2019).
13 Chen, C., Gu, H. & Liu, S. Ultra-simplified diffraction-based computational spectrometer. *Light: Science & Applications* **13**, 9 (2024).
14 Zhang, Z., Xiao, S., Song, Q. & Xu, K. Scalable on-chip diffractive speckle spectrometer with high spectral channel density. *Light: Science & Applications* **14**, 130 (2025).
15 Calafiore, G. *et al.* Holographic planar lightwave circuit for on-chip spectroscopy. *Light: Science & Applications* **3**, e203-e203 (2014).
16 Li, Y. *et al.* A platform for integrated spectrometers based on solution-processable semiconductors. *Light: Science & Applications* **12**, 184 (2023).
17 Chai, J. *et al.* A MEMS Based Fourier Transform Spectrometer and Its Scan Stability Study. *ECS J. Solid State Sci. Technol.* **7**, Q3025-Q3031 (2018).
18 Wang, D. *et al.* Fourier transform infrared spectrometer based on an electrothermal MEMS mirror. *Appl. Optics* **57**, 5956-5961 (2018).
19 Wang, D. *et al.* Nondestructive On-Site Detection of Soybean Contents Based on An Electrothermal MEMS Fourier Transform Spectrometer. *IEEE Photonics Journal* **11**, 1-10 (2019).
20 Chen, H. *et al.* H∞ Robust Control of a Large-piston MEMS Micromirror for Compact Fourier Transform Spectrometer Systems. *Sensors* **18**, 22 (2018).
21 Han, F., Wang, W., Zhang, X. & Xie, H. Miniature Fourier Transform Spectrometer with a Dual Closed-loop Controlled Electrothermal Micromirror. *Opt. Express* **24**, 22650-22660 (2016).
22 Jain, A. & Huikai, X. An electrothermal microlens scanner with low-voltage large-vertical-displacement actuation. *IEEE Photonics Technol. Lett.* **17**, 1971-1973 (2005).
23 Todd, S. T., Jain, A., Qu, H. & Xie, H. A multi-degree-of-freedom micromirror utilizing inverted-series-connected bimorph actuators. *Journal of Optics A: Pure and Applied Optics* **8**, S352 (2006).
24 Todd, S. T. & Xie, H. An Electrothermomechanical Lumped Element Model of an Electrothermal Bimorph Actuator. *J. Microelectromech. Syst.* **17**, 213-225 (2008).
25 Pal, S. & Xie, H. Distributed and lumped element models for a bimorph-actuated micromirror. *J. Micromech. Microeng.* **20**, 045020 (2010).
26 Pal, S. & Xie, H. Repeatability Study of an Electrothermally Actuated Micromirror.in *47th Annual IEEE International Reliability Physics Symposium.* 549-556 (IEEE, 2009).
27 Birla, M. *et al.* Multi-photon 3D Imaging with an Electrothermal Actuator with Low Thermal and Inertial Mass. *Sensors and Actuators A: Physical* **329**, 112791 (2021).
28 Zhou, L., Zhang, X. & Xie, H. An Electrothermal Cu/W Bimorph Tip-tilt-piston MEMS Mirror with High Reliability. *Micromachines* **10**, 14 (2019).
29 Pal, S. & Xie, H. Fabrication of Robust Electrothermal MEMS Devices Using Aluminum-

Tungsten Bimorphs and Polyimide Thermal Isolation. *J. Micromech. Microeng.* **22**, 14 (2012).
30 Yang, H. *et al.* A robust lateral shift free (LSF) electrothermal micromirror with flexible multimorph beams. *Microsyst. Nanoeng.* **9**, 12 (2023).
31 Wu, L., Pais, A., Samuelson, S., Guo, S. & Xie, H. A Mirror-tilt-insensitive Fourier Transform Spectrometer Based on a Large Vertical Displacement Micromirror with Dual Reflective Surface.in *The 15th International Solid-State Sensors, Actuators and Microsystems Conference (Transducers).* 2090-2093 (IEEE).
32 Wu, L. & Xie, H. A large vertical displacement electrothermal bimorph microactuator with very small lateral shift. *Sens. Actuator A-Phys.* **145**, 371-379 (2008).
33 Jia, K., Pal, S. & Xie, H. An Electrothermal Tip-Tilt-Piston Micromirror Based on Folded Dual S-Shaped Bimorphs. *J. Microelectromech. Syst.* **18**, 1004-1015 (2009).
34 Liu, L., Pal, S. & Xie, H. MEMS Mirrors Based on A Curved Concentric Electrothermal Actuator. *Sens. Actuator A-Phys.* **188**, 349-358 (2012).
35 Liu, L. & Xie, H. 3-D Confocal Laser Scanning Microscopy Based on a Full-MEMS Scanning System. *IEEE Photonics Technol. Lett.* **25**, 1478-1480 (2013).
36 Samuelson, S. & Xie, H. A Large Piston Displacement MEMS Mirror with Electrothermal Ladder Actuator Arrays for Ultra-low Tilt Applications. *J. Microelectromech. Syst.* **23**, 39-49 (2014).
37 Liu, L. *et al.* MEMS-based 3D Confocal Scanning Microendoscope Using MEMS Scanners for Both Lateral and Axial Scan. *Sensors and Actuators A: Physical* **215**, 89-95 (2014).
38 Wang, W., Chen, J., Zivkovic, A., Tanguy, Q. & Xie, H. A Compact Fourier Transform Spectrometer on a Silicon Optical Bench With an Electrothermal MEMS Mirror. *J. Microelectromech. Syst.* **25**, 347-355 (2016).
39 Wang, W., Chen, J., Zivkovic, A. & Xie, H. A Fourier Transform Spectrometer Based on an Electrothermal MEMS Mirror with Improved Linear Scan Range. *Sensors* **16**, 13 (2016).
40 Wang, W., Samuelson, S., Chen, J. & Xie, H. Miniaturizing Fourier Transform Spectrometer with an Electrothermal Micromirror. *IEEE Photonics Technol. Lett.* **27**, 1418-1421 (2015).
41 Zhou, L., Yu, X., Feng, P., Li, J. & Xie, H. A MEMS Lens Scanner Based on Serpentine Electrothermal Bimorph Actuators for Large Axial Tuning. *Opt. Express* **28**, 23439-23453 (2020).
42 Sun, J. *et al.* 3D in vivo optical coherence tomography based on a low-voltage, large-scan-range 2D MEMS mirror. *Opt. Express* **18**, 12065-12075 (2010).
43 Li, M., Chen, Q., Liu, Y., Ding, Y. & Xie, H. Modelling and Experimental Verification of Step Response Overshoot Removal in Electrothermally-actuated MEMS Mirrors. *Micromachines* **8**, 11 (2017).
44 Fang, X. Y. *et al.* Destructive Reliability Analysis of Electromagnetic MEMS Micromirror Under Vibration Environment. *IEEE Journal of Selected Topics in Quantum Electronics* **28**, 1-8 (2022).
45 HAMAMATSU. *https://www.hamamatsu.com.cn/cn/zh-cn/product/optical-sensors/spectrometers/ftir-engine/measurement-example.html* (2020)

Supplementary Files

This is a list of supplementary files associated with this preprint. Click to download.

- SupplementaryVideo1.mp4
- SupplementInformation.pdf